

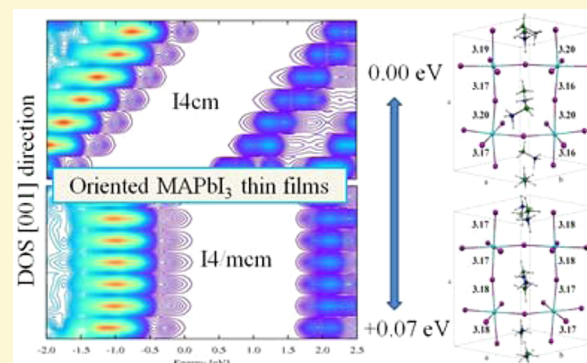
# Interplay of Orientational Order and Electronic Structure in Methylammonium Lead Iodide: Implications for Solar Cell Operation

Claudio Quarti,<sup>§</sup> Edoardo Mosconi,<sup>§</sup> and Filippo De Angelis\*

Computational Laboratory for Hybrid/Organic Photovoltaics (CLHYO), Istituto di Scienze e Tecnologie Molecolari (CNR-ISTM), Via Elce di Sotto 8, I-06123, Perugia, Italy

 Supporting Information

**ABSTRACT:** We report on ab initio electronic structure and Car-Parrinello molecular dynamics simulations for several structural models of the prototype  $\text{MAPbI}_3$  perovskite for solar cells applications. We considered both configurations having a preferred orientation of the MA cations, giving rise to a net dipole alignment, and configurations with an isotropic distribution of the MA cations, respectively representative of polar (ferroelectric) and apolar (antiferroelectric) structures. Our calculations demonstrate the preferred stability of a set of polar structures over apolar ones, with an energy difference within 0.1 eV and a conversion barrier within 0.2 eV per unit cell (four  $\text{MAPbI}_3$ ), thus possibly accessible at room temperature. Ferroelectric-like orientations lead to a quasi  $I4cm$  structure for the inorganic component, characterized by lack of inversion symmetry, while the antiferroelectric-like orientations are associated to a quasi  $I4/mcm$  structure. Ab initio molecular dynamics simulations on the polar structures show no molecular rotations in the investigated time-scale, while several MA rotations are observed in the same time scale for the considered apolar structure, which is thus characterized by a higher disorder. The  $I4cm$  and  $I4/mcm$  types of structure have markedly different band structures, despite showing a relatively small band gap variation. Simulations carried out on finite surface slabs demonstrate that a net orientation of the MA cations gives rise to a strong bending in the valence and conduction bands, which could definitely assist charge separation and reduce carrier recombination, provided one is able to effectively stabilize polar compared to apolar structures. We believe our results could contribute an important step toward an in-depth comprehension of the basic properties of organohalide perovskites, assisting a further optimization of their photovoltaic response.



## 1. INTRODUCTION

Hybrid lead–halide perovskites have recently emerged as new promising materials in the field of photovoltaics, thanks to their unique set of properties, such as small and tunable band gap,<sup>1</sup> ambipolar charge transport properties,<sup>2,3</sup> limited charge recombination,<sup>4–6</sup> and joined with the possibility to employ low-cost solution techniques for their production. This class of materials has been long time known and studied in relation to their very peculiar dielectric properties,<sup>7</sup> but the first application of organohalide perovskites in photovoltaics traces back to 2009, with the work of Kojima et al.<sup>8</sup> In just a few years, the number of applications of hybrid lead–halide perovskites in photovoltaics increased exponentially, reaching a certified 17.9% efficiency, and exploring several device concepts and configurations and testing different production techniques.<sup>9–19</sup>

In spite of the amount of papers published on the application of this class of materials for solar cells, an in-depth understanding of the physical mechanisms lying at the basis of the high performance of hybrid perovskite is still to be achieved. Only recently, fundamental aspects such as, for instance, the role of the chlorine doping in the photovoltaic operational mechanism,<sup>4</sup> the Raman<sup>20</sup> and IR spectroscopic

response<sup>21</sup> of these materials, and the nature of the photo-generated species<sup>22</sup> have been elucidated. A clear peculiarity of hybrid lead–halide perovskites is the presence of organic cations, e.g., methylammonium (MA) in the prototypical  $\text{MAPbI}_3$  case, embedded within the cuboctahedral cavity formed by the inorganic  $\text{PbI}_6$  octahedra. Ab initio calculations demonstrated that the MA cation is not involved in the frontier orbitals,<sup>23,24</sup> but, in spite of this, the presence of mobile ions within the inorganic cage and their possible dynamics is expected to play an important role in the structural<sup>25</sup> and dielectric properties of this class of materials.<sup>26–28</sup> In this regard, we recently demonstrated the importance of the MA cation dynamics, coupling with the inorganic lattice, on the electronic properties of the cubic  $\text{MAPbI}_3$  perovskite.<sup>21</sup> Stoumpos et al. suggested that this material exhibits a ferroelectric response to an externally applied electric field,<sup>29</sup> recently confirmed by Kutes et al.,<sup>30</sup> whose implications in photovoltaics are considered with strong interest. In particular,

Received: August 31, 2014

Revised: October 20, 2014

Published: October 21, 2014

it is believed that the ferroelectric effect significantly promotes the charge separation and may ultimately increase the solar cells efficiency.<sup>31</sup> Notably, a correlation between the structure, polarization orientation, and electronic structure of an all-inorganic perovskite oxide has been very recently reported in the literature.<sup>32</sup>

The orientation of the organic cations is probably the most complex problem in the structural characterization of hybrid organohalide perovskites. In the low temperature MAPbI<sub>3</sub> orthorhombic phase, the position of the MA cations was solved, showing these are oriented in a head-to-tail fashion such to maximize the hydrogen bonding with the iodine atoms.<sup>33–35</sup> The first symmetry assignment of the low temperature phase of the MAPbX<sub>3</sub> perovskites by Poglitsch and Weber excluded the presence of inversion symmetry in these systems. The *P221*<sub>1</sub> and *Pna2*<sub>1</sub> space groups were proposed for MAPbCl<sub>3</sub> and for both MAPbBr<sub>3</sub> and MAPbI<sub>3</sub>, respectively.<sup>7</sup> Later, Swainson et al. revised these assignments, proposing the *Pnma* space group for both MAPbCl<sub>3</sub><sup>34</sup> and MAPbBr<sub>3</sub>,<sup>33</sup> thus excluding possible ferroelectric properties for the low temperature phase of these materials. Baikie et al. have recently demonstrated that the orthorhombic phase of MAPbI<sub>3</sub> also belongs to the *Pnma* space group.<sup>35</sup> In the high temperature cubic phase of MAPbX<sub>3</sub> perovskites, instead, the MA cations are dynamically disordered, moving in an isotropic potential at a rate approaching that of the freely rotating MA cation.<sup>36</sup> The tetragonal phase of the MAPbX<sub>3</sub> perovskites is expected to be somehow in between the orthorhombic and cubic phases. In this phase, stable at room temperature for MAPbI<sub>3</sub>, the inorganic structure shows a characteristic octahedral tilting of the type  $a^0a^0c^-$ ,<sup>29,37</sup> following the Glazer notation.<sup>38</sup> The assignment of the space group symmetry of this system is quite debated. Poglitsch and Weber proposed the *I4/mcm* space group,<sup>7</sup> while Stoumpos et al. more recently proposed the noncentrosymmetric *I4cm* space group,<sup>29</sup> which is consistent with the observed ferroelectric behavior. However, it is worth mentioning that the  $C_{3v}$  symmetry of the MA cation prevents the formation of genuinely symmetric structures belonging to both space groups. Early calorimetric studies by Knop et al.<sup>36</sup> and Onoda-Yamamuro et al.<sup>26</sup> have highlighted that the orthorhombic to tetragonal phase transition in MAPbX<sub>3</sub> perovskites has large transition entropies, indicating that the transition is accompanied by a partial disordering of the MA cations. This was confirmed by measurements of the dielectric constant by Onoda-Yamamuro et al.<sup>26</sup> which detected a sudden variation of the dielectric constant of the MAPbX<sub>3</sub> perovskites at the orthorhombic to tetragonal transition. Nevertheless, it was suggested that in the tetragonal phase the MA cations still possess preferred orientations<sup>36</sup> and a certain degree of long-range order.<sup>26</sup> Despite many attempts, the crystal structure of MAPbI<sub>3</sub> has not been fully solved, thus preventing at least in part an atomistic understanding of its superior photovoltaic properties by means of structure/property relations.

In light of the potential impact of the orientational order of the organic cations on the perovskites properties, in particular in relation to their extremely successful application in photovoltaics, we present here a systematic investigation of the interplay between the arrangement of the MA cations and the structural and electronic properties of MAPbI<sub>3</sub>, the prototype hybrid perovskite for photovoltaic applications. We investigated several orientational configurations of the organic cations by first-principles electronic structures calculations, integrated by first-principle molecular dynamics simulations.

Most of the properties of the MAPbI<sub>3</sub> perovskite have been studied up to now with ab initio methods on the basis of a simple cubic model.<sup>27,39–44</sup> We adopt here the tetragonal MAPbI<sub>3</sub> unit cell, corresponding to the room temperature stable phase,<sup>45</sup> and consider both configurations showing a net resulting orientation of the MA cations, which are likely to present ferroelectric properties, and configurations in which the MA cations show an isotropic distribution of their orientation. Geometry optimizations are performed to evaluate the relative structural stability and to establish the possible effect of the MA orientation on the electronic properties of the MAPbI<sub>3</sub> perovskite. Ab initio molecular dynamics simulations are then employed to investigate the dynamics of the MA cations in the tetragonal MAPbI<sub>3</sub> perovskite at room temperature and, in particular, the possible interconversion among various possible structures in conditions close to the operative ones. The impact of the underneath structural features on charge separation and recombination in MAPbI<sub>3</sub> thin films are also assessed.

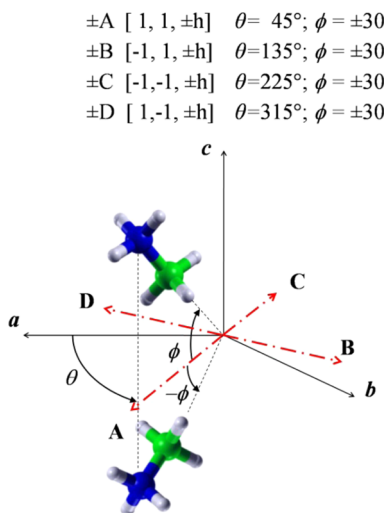
We find that polar structures, with the MA cations partly oriented along the [001] direction, are favored over apolar structures by less than 0.1 eV per unit cell (four MAPbI<sub>3</sub> units). The internal field generated by the MA cations in these structures gives rise to strong band bending in thin films, which may definitely assist charge separation of photogenerated charge carriers. We also find that structures with octahedra tilting along the [001] and [110] directions lie within the same 0.1 eV energy range, with a conversion barrier of less than 0.2 eV among the two types of tilted structures. The picture extracted from our calculations thus reveals a ferroelectric-like arrangement of the MA cations as the most stable configuration but also suggests a potentially disordered arrangement of the PbI<sub>6</sub> octahedra, which may dynamically interconvert at room temperature.

## 2. MODELS AND METHODS

In previous DFT calculations on MAPbI<sub>3</sub>,<sup>20,25,28,46</sup> it was observed that MAPbI<sub>3</sub> in the tetragonal phase shows a typical  $a^0a^0c^-$  tilting of the octahedra. In this type of structure, the MA cations are arranged along specific directions, i.e., roughly along the direction connecting the two opposite faces of the pseudocubic cell, with a small tilting with respect to the *ab* plane. This orientation was confirmed also by Filippetti and Mattoni,<sup>47</sup> and it is likely to be due to the formation of a stronger hydrogen bonding network. The classification of the orientation of the MA cation in the MAPbI<sub>3</sub> perovskite is reported in Scheme 1. With respect to the *ab*-plane of the tetragonal structure, the MA cations can be oriented along the [110], [ $\bar{1}10$ ], [ $1\bar{1}0$ ], and [ $1\bar{1}\bar{0}$ ] directions, which correspond the molecules lying within the *ab*-plane with angles of  $\theta = 45^\circ, 135^\circ, 225^\circ$ , and  $315^\circ$  with respect to the *a*-axis; see Scheme 1. With respect to the *c*-axis, the molecules have two symmetric preferred orientations,  $\phi = \pm 30^\circ$ , where  $\phi$  measures the angle formed by the CN axis with the *ab*-plane. The orientation of the MA cation is thus fully described by the  $\theta$  and  $\phi$  angles. In this work, the orientation of the MA cation within the plane is labeled as A, B, C, and D, corresponding respectively to  $\theta = 45^\circ, 135^\circ, 225^\circ$ , and  $315^\circ$ , while the angle with respect to the *ab*-plane is indicated by the sign + ( $\phi \sim +30^\circ$ ) and – ( $\phi \sim -30^\circ$ ). This classification is depicted in Scheme 1.

Starting from the established  $a^0a^0c^-$  structure for the inorganic framework, we investigated up to nine guess structures, characterized by either a global preferential orientation or a global isotropic orientation of the MA cations, the former and the latter being representative of polar and apolar structures. The present structures are labeled with numbers going from 1 to 9. In addition, we investigated the structural model proposed by Stoumpos et al. by X-ray diffraction,<sup>29</sup> characterized by a parallel ordering of the MA cations along the *c*-axis, hereafter structure 10. All the guess structures have

**Scheme 1. Preferred Orientations of the Organic Cation within the Perovskite Cavity<sup>a</sup>**



<sup>a</sup> *a*, *b*, and *c* are the crystallography axes of the perovskite in the tetragonal phase, where the octahedral tilting is along the *c*-axis, i.e., along the [001] direction. A, B, C, and D represent the projection of the MA cation orientations within the *ab* plane, as measured by the angle  $\theta$ . The tilting of the molecule with respect to the *c*-axis is measured by the  $\phi$  angle.

been fully optimized by DFT without any symmetry constraints, and their stability and electronic properties have been studied.

To investigate the dynamics of the MA cations in the MAPbI<sub>3</sub> perovskite, we have carried out CPMD simulations on two guess structures: (i) structure 1, which has an isotropic distribution of the MA cations in  $\theta$  but shows all the molecules tilted with the same  $\phi$  angle; and (ii) structure 4, showing an isotropic distribution in both angles. The molecular orientation of the four MA cations in the various investigated structures and the presence of a global preferred orientation are summarized in Table 1.

DFT calculations within periodic boundary conditions, have been performed with a planewave/pseudopotential approach, as implemented in the PWSCF package of quantum-espresso,<sup>48</sup> on the tetragonal unit cell of MAPbI<sub>3</sub>, containing 48 atoms and 4 MA cations

**Table 1. Orientation of the MA Cations in the Various Structural Models Investigated and Resulting Net Molecular Alignment<sup>a</sup>**

structure	cation orientation				resulting MA dipole direction
	A	B	C	D	
1	1-	1-	1-	1-	[001]
2	1-	1-; 1-	1-		[1̄10] [001]
3	2-	2-			[010] [001]
4	1+	1-	1-	1+	---
5	2+		2-		---
6	1+; 1-		1+; 1-		---
7	1+; 1-		1+; 1-		---
8 <sup>b</sup>	1+; 1-		1+; 1-		---
9 <sup>b</sup>	2-		2-		---
10 <sup>c</sup>					[001]

<sup>a</sup>The molecular orientation is labeled as indicated in Scheme 1. <sup>b</sup>For structures 8 and 9 the *c* axis is rotated along the [110] direction. <sup>c</sup>In structure 10, the MA cations are oriented along the *c* axis, so this structure does not show any projection of the MA axis on the *ab* plane.

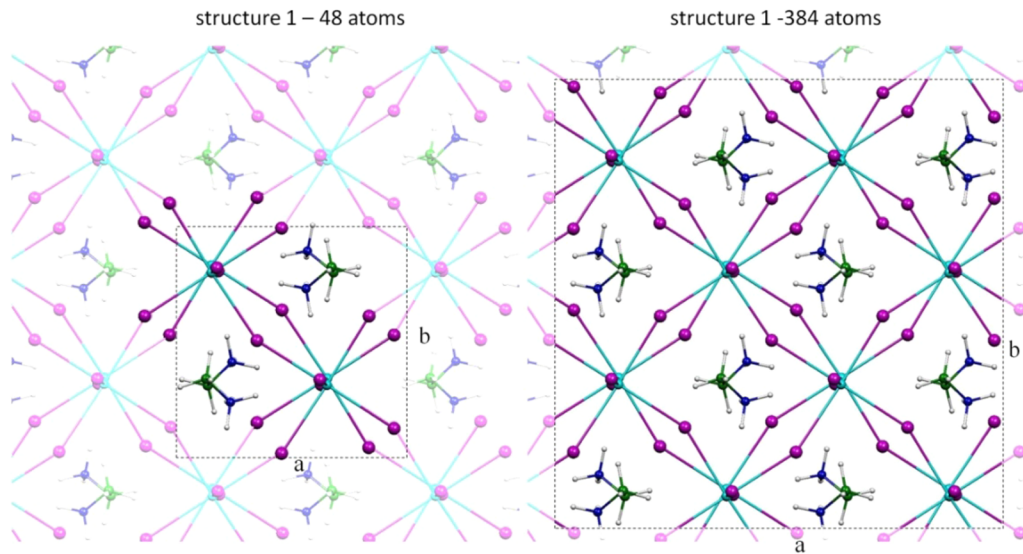
(see left panel of Scheme 2). The PBE exchange-correlation functional<sup>49</sup> is used along with ultrasoft,<sup>50</sup> scalar relativistic pseudopotentials for all atoms. A *k*-point mesh of  $4 \times 4 \times 4$  and two sets of cutoffs, 25–200 Ry and 50–400 Ry, are adopted, respectively, for the sampling of the first Brillouin zone and the expansion of the wave function and density. We performed structural optimizations both with cell parameters fixed to the experimental values reported by Poglisch and Weber<sup>7</sup> and relaxing both the atomic positions and the cell parameters. The electronic structure has been calculated considering also spin-orbit coupling (SOC) effects<sup>43</sup> with 25–200 Ry cutoff, on the scalar relativistic (SR) optimized geometries. The effect of dispersion interactions in geometry optimizations was also investigated in selected cases.

CPMD simulations are performed within the Car-Parrinello method employing ultrasoft pseudopotentials,<sup>51,52</sup> as implemented in the Quantum Espresso package.<sup>48</sup> These calculations are carried out on a  $2 \times 2 \times 2$  supercell of the tetragonal unit (384 atoms and 32 MA cations, right panel of Scheme 2). The Hamiltonian parameters are the same of those used for the static calculations and in our previous work:<sup>21</sup> PBE exchange correlation functional, 25–200 Ry cutoff for the expansion wave function density. CPMD simulations are performed at the  $\Gamma$  point of the first Brillouin zone. Cell parameters are fixed in this case to the experimental values.<sup>7</sup> We used an integration time step of 5 au, together with a fictitious electronic mass of 400 au and the real ionic masses, except for hydrogen atoms, which have been replaced by deuterium for computational convenience. CPMD simulations were conducted at  $\sim$ 320 K for a total simulation time of  $\sim$ 12 ps after a few picoseconds of thermal equilibration.

### 3. RESULTS AND DISCUSSION

**3.1. Structural and Electronic Properties.** During the DFT optimization, all the guess structures roughly preserved the original orientation of the MA cations reported in Table 1, i.e., the  $\theta$  and  $\phi$  angles slightly varied but without undergoing a transition among the various initial orientations, which therefore represent local minima on the potential energy surface. The optimized geometries of the considered structural models are depicted in Figure 1. The relative energies, band-gaps (all direct band-gaps at the  $\Gamma$  point), and structural parameters of the various relaxed structures are summarized in Table 2. As previously noted, SR-DFT fortuitously delivers calculated band gap values for lead-halide perovskite in good agreement with experiment, due to cancellation of SOC and many-body correlation effects.<sup>25</sup> Introduction of SOC within DFT delivers strongly reduced band-gaps,<sup>43</sup> which are properly corrected at the SOC-GW level<sup>39,53</sup> or adopting hybrid functionals.<sup>54</sup> It also has to be noticed that the effect of SOC is structure-dependent, as recently reported by us,<sup>28</sup> with SOC-DFT band-gaps qualitatively following the results of the more computationally demanding SOC-GW calculations.<sup>53</sup>

We first focus on the relative stability of the various structures. As shown in Table 2, the isoenergetic structures 1–3 are the most stable among the investigated series. All the other structures, with the exception of structure 10, are found within 0.05–0.10 eV per unit cell from 1–3, i.e., only slightly larger than kT at the room temperature ( $\sim$ 0.03 eV). Notably, structures 8 and 9 show the tilting of the PbI<sub>6</sub> octahedra along the [110] rather than along the conventional [001] crystallographic direction. In other words, in these two structures the *c* axis is rotated along the [110] direction. This behavior probably reflects the soft nature of this class of materials, which can accommodate relatively large structural distortions at a small energy cost. The optimized structure 10, having the MA cations aligned along the *c*-axis, does not show the typical  $a^0a^0c^-$  octahedra tilting, Figure 1. In addition, the resulting structure is

**Scheme 2. Structural Models Employed in the Present Work<sup>a</sup>**

<sup>a</sup>48-atoms model was adopted for the static DFT calculations (left panel) and 384-atoms model for the CPMD calculations (right panel). The simulation cell and the crystallographic *a* and *b* axes are highlighted.

strongly destabilized, lying about 0.5 eV above the most stable **1–3** structures. The present results are not altered when the cell parameters are allowed to relax together with the atomic positions, Table 2, and/or when larger cutoffs and dispersion interactions are considered, see Table SI1, Supporting Information. Our calculations thus show that in MAPbI<sub>3</sub> a tilted orientation of the MA cations with respect to the *ab*-plane with  $\phi \sim 30^\circ$ , as such corresponding to structures **1–3**, is energetically preferred. Preliminary results indicate a ferroelectric polarization of  $4.4 \mu\text{C}/\text{cm}^2$  for structure **1**, thus about a factor 8 smaller than the value reported in ref 40.

It is worth noting that, together with a different orientation of the MA cations, the various structures show also a different structure of the inorganic framework, Figure 1. The oriented structures **1**, **2**, **3**, **9**, and **10** show an “in-phase” alternation of the apical Pb–I bond lengths, which is consistent with the *I4cm* space group proposed by Stoumpos et al.<sup>29</sup> Such bond length alternation is maximized in structure **10** ( $\sim 0.2 \text{ \AA}$ ), in relation to the alignment of the MA cations along the *c*-axis peculiar for this structure. At the opposite, the isotropic structures **4**, **5**, and **8** show an “out-of phase” alternation or no alternation of the apical Pb–I bond lengths, which is consistent with the *I4/mcm* space group proposed by Poglitsch and Weber.<sup>7</sup> Summarizing, the orientation of the MA cations in the MAPbI<sub>3</sub> perovskite strongly influences the inorganic structure, with a ferroelectric-like/antiferroelectric-like structure coherent with an *I4cm* or *I4/mcm* space group symmetry.

Notably, the different cation orientations deliver substantially different calculated cell parameters, Table 2. In particular, structures **1–7** all provide similar cell parameters, with  $a \approx b$  values shorter than experiment ( $8.86 \text{ \AA}$ ) and *c* values longer than experiment ( $12.66 \text{ \AA}$ ), leading to a *c/a* ratio of  $\sim 1.46$ , against the  $\sim 1.43$  experimental ratio. Structures **8** and **9**, instead, show a reverse trend, with elongated  $a \approx b$  values and shorter *c* values, leading to a *c/a* ratio of  $\sim 1.41$ . This is obviously related to the different octahedra tilting directions of the two types of structures. Notably, the two different tilting directions are found to lie within less than 0.1 eV. The situation does not change when moving to higher plane wave/density

cutoffs, Supporting Information, although an overall lengthening of cell parameters was found in this case, consistent with the analysis of ref 55. Recent calculations demonstrated that inclusion of van der Waals interactions delivered calculated cell parameters of MAPbI<sub>3</sub> in better agreement with experimental values.<sup>55–58</sup> When accounting for dispersion interactions, see data for selected structures in Supporting Information, the calculated cell parameters decreased, as expected, but neither the relative stability order nor the main structural features, e.g., the *c/a* ratio, were significantly affected. Similarly, the calculated SR-DFT band-gaps all decreased by ca. 0.1 eV, by virtue of the volume contraction, but their trends with cation orientation remained unchanged. This is in line with the report by Geng et al., who pointed out that, even accounting for dispersion interactions, the computed cell parameters still sizably depend on the orientation of the organic cations.<sup>54</sup> On overall, our calculated trends with cation orientation seem sufficiently robust with respect to variations in the level of theory to allow us to effectively discuss the interplay of cation orientation and electronic structure.

We now discuss the effects of the molecular orientation on the electronic properties of MAPbI<sub>3</sub>. As shown in Table 1, for all the considered structures except **6** and **9**, the orientation of the MA cations affects the SOC-DFT band gap value within a range of 0.14 eV at fixed cell parameters. SR-DFT band-gaps show a reduced variability compared to SOC-DFT results, due to the aforementioned interplay of structural features and SOC effects.<sup>28</sup> Structure **9** (**6**) shows a notable band gap increase (decrease), by  $\sim 0.2$  eV compared to the more stable structures **1–3**, despite being only 0.07 (0.06) eV higher in energy. These results highlight the large variability in band gap values that could be observed if one were able to selectively obtain one type of structure.

The orientation of the MA cations, inducing the consequent adaptation of the inorganic framework, has important consequences for the electronic properties of the MAPbI<sub>3</sub> perovskite. Considering here structures **1**, **3**, and **10**, as representative of the oriented structures, and structure **4**, as representative of the isotropic structures, we computed the

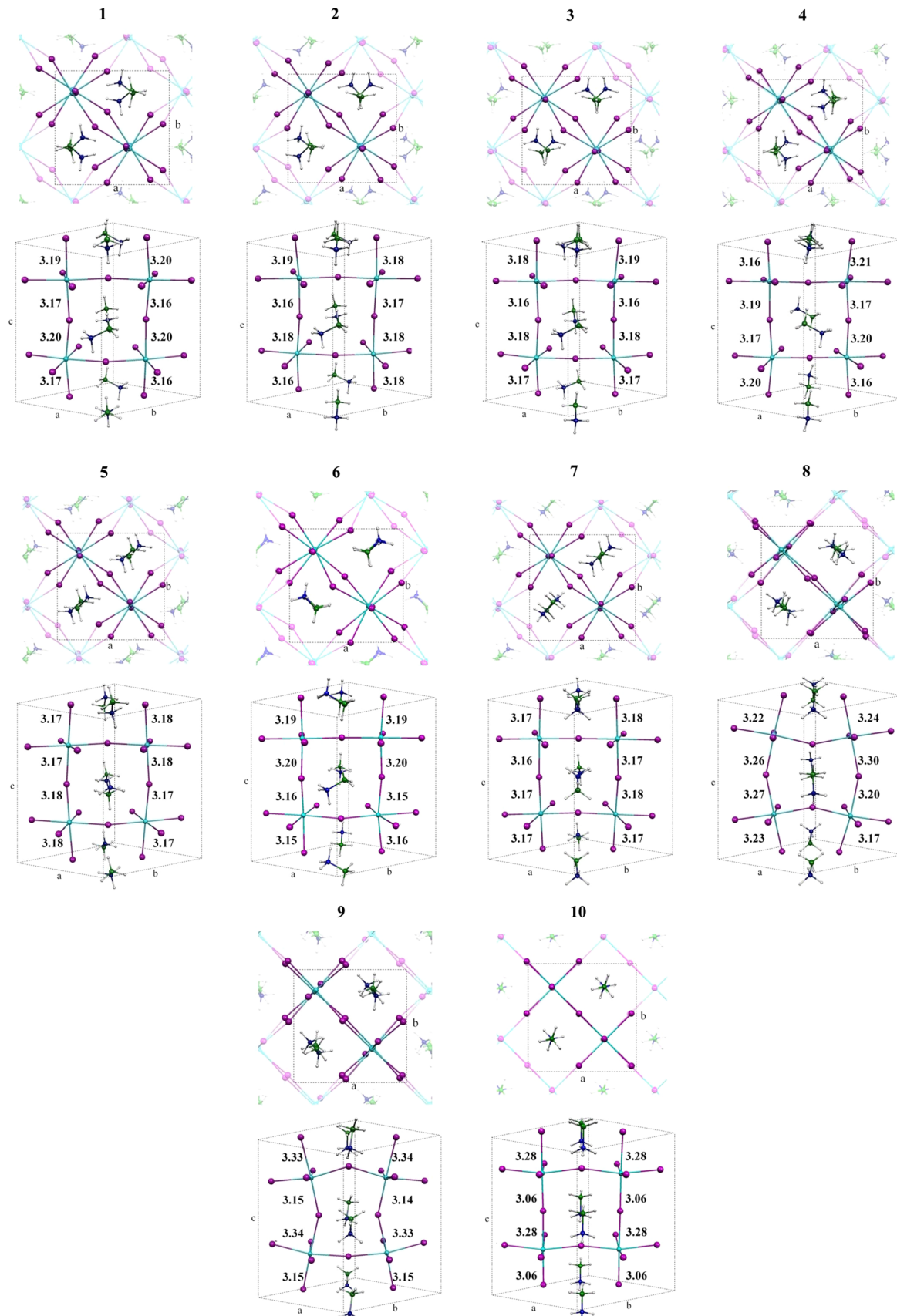


**Figure 1.** Optimized structures 1–10 along with main bond distances ( $\text{\AA}$ ). For each structure, we report the view along the [001] and [110] directions.

**Table 2.** Relative Energy ( $\Delta E$ , eV), Scalar Relativistic (SR) and Spin–Orbit (SOC) Band Gaps ( $E_g$ , eV) and Cell Parameters ( $a$ ,  $b$ ,  $c$ , Å) for All the Investigated Structures<sup>a</sup>

struct.	MA orient.	expt. cell parameters			optimized cell parameters		
		$\Delta E$	$E_g$ (SR)	$E_g$ (SOC)	$a, b, c$	rel. en.	$E_g$ (SR)
1	−D, −A, −C, −B	0.00	1.57	0.53	8.75, 8.74, 12.77	0.02	1.47
2	−B, −A, −C, −B	0.00	1.59	0.57	8.75, 8.73, 12.79	0.00	1.48
3	−B, −A, −A, −B	0.01	1.62	0.60	8.74, 8.73, 12.80	0.00	1.50
4	−B, −C, +D, +A	0.09	1.60	0.53	8.76, 8.74, 12.75	0.11	1.51
5	+A, −C, −C, +A	0.09	1.57	0.51	8.76, 8.72, 12.80	0.08	1.50
6	+A, −A, +D, −D	0.06	1.34	0.30	8.78, 8.77, 12.71	0.08	1.22
7	+C, −A, −C, +A	0.06	1.54	0.48	8.77, 8.77, 12.70	0.11	1.46
8	−C, −A, +A, +C	0.08	1.60	0.46	8.85, 8.86, 12.46	0.11	1.56
9	−A, −C, −C, −A	0.07	1.82	0.80	8.86, 8.81, 12.54	0.10	1.74
10 <sup>b</sup>	-----	0.47	1.61	0.58	8.85, 8.85, 12.71	0.39	1.62

<sup>a</sup>For each structure, the orientation of the organic cations is reported (MA orient) in relation to the labels of Scheme 1. Data are presented for calculations at both experimental and optimized cell parameters. For the latter, also the optimized cell parameters are reported. <sup>b</sup>In structure 10 the MA cations are aligned along the  $c$ -axis, so they have no projection on the  $ab$  plane.

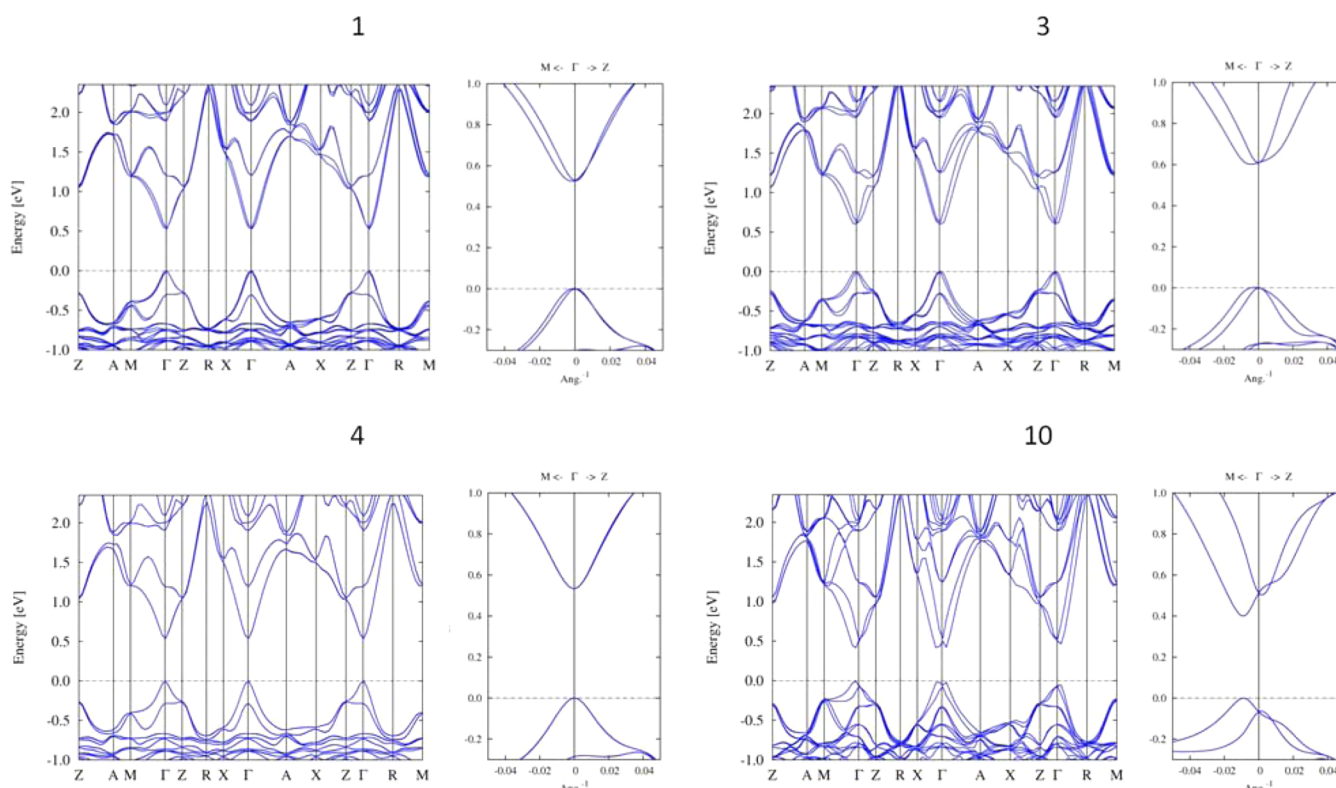


**Figure 2.** SOC-DFT calculated band structure in the first Brillouin zone (left panels) and magnification of the region around the  $M \rightarrow \Gamma \rightarrow Z$  direction (right panels) for structures 1, 3, and 10 (ferroelectric-like) and for structure 4 (antiferroelectric-like).

SOC-DFT band structure, Figure 2. We observe that, in spite of the general similarity of both the band gap (see Table 2) and of the band structures, we can still retrieve significant differences. A  $k$ -point splitting of the frontier orbitals near the  $\Gamma$  point is observed in the oriented structures 1, 3, and 10, which is absent in the isotropic structure 4. The same result is found for all the investigated structures (see Supporting Information Figure S11). Previous calculations by Kim et al.<sup>44</sup> and by us<sup>28</sup> already pointed out this phenomenon, namely a Rashba/Dresselhaus effect in the tetragonal phase of the  $\text{MAPbI}_3$  perovskite. Thus, in the present work we confirm the presence of this effect in the tetragonal phase of  $\text{MAPbI}_3$  and, most notably, we demonstrate the dependence of the Rashba/Dresselhaus effect on the orientation of the MA cations. In particular, the splitting of the bands is

larger in structures with a large degree of alignment of the molecules, while it is nearly null when the molecules are not aligned, i.e., when the structure is more “centro-symmetric”, consistently with the selection rules associated with this effect.

The effective masses for both electrons and holes, calculated by parabolic fitting of the SOC-DFT bands, and the reduced masses calculated for the various structures are summarized in Supporting Information. In general, the orientation of the molecules does not significantly affect the transport properties in  $\text{MAPbI}_3$ , except in the case of structures 8 and 9. For all the structures, the electrons are calculated to have smaller effective masses than the holes. In the case of structures 8 and 9 instead, the electrons show a slightly larger mass (+50%) than those found in the other structures, while the masses of the holes are

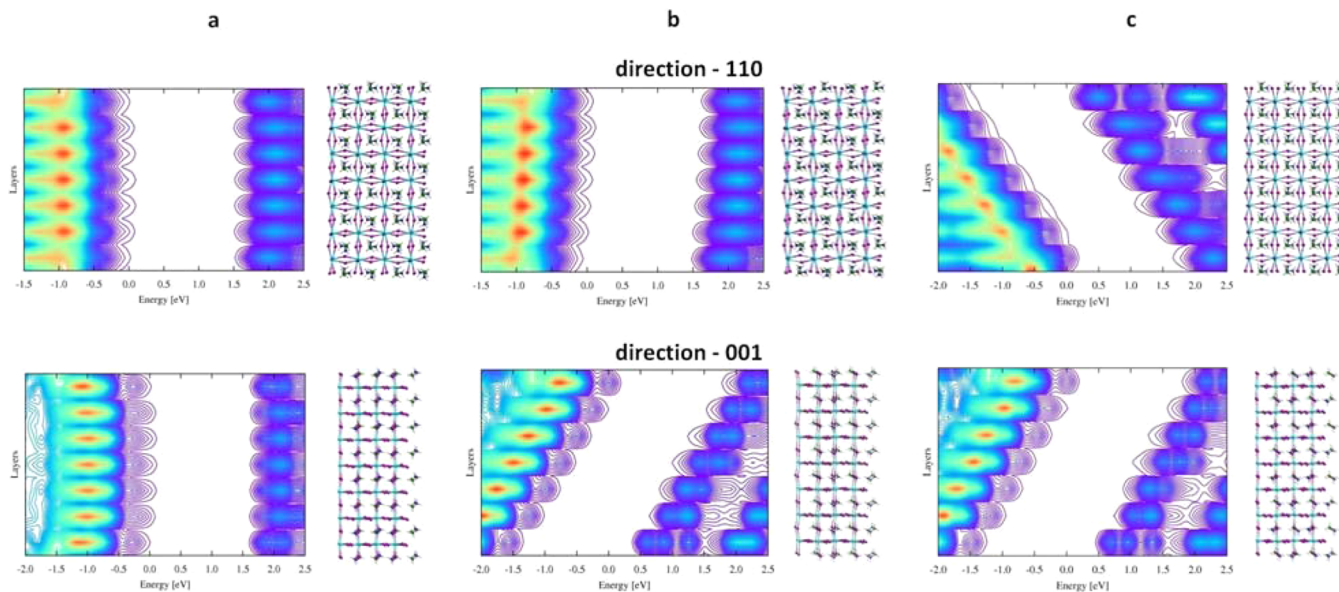


**Figure 3.** Surface plot of the SR-DFT density of states of the valence and conduction band for the layer models obtained from (a) structure 4 (no net orientation of the MA cations); (b) structure 1 (net orientation of the MA cations along the [001] direction); and (c) structure 3 (net orientation of the MA cations along [010] and [001]). The upper and the lower panels show the DOS of the finite slab along the [110] and the [001] direction, respectively.

2–3 times larger than the masses of the other structures. This data clearly shows the variability in electronic properties associated with a particular MA orientation, despite the similar structural energetics.

**3.2. Effect of MA Orientation in Thin Films.** To investigate the possible effect of the MA orientation on the properties of perovskite thin films, we have constructed finite slab models of  $\text{MAPbI}_3$  surfaces as follows. The optimized tetragonal unit cell is replicated along the [110] and the [001] directions, for a total length of six pseudocubic units along these directions (see right panels in Figure 3). We set a vacuum of  $\sim 15 \text{ \AA}$  between one layer and its periodic replica in the supercell. No relaxation of the surface slabs was considered, retaining the geometry optimized in periodic boundary conditions. This analysis was performed for the three representative structures 1, 3, and 4, having a net orientation of the molecules along the  $c$ -axis, along both the  $c$ -axis and parallel to the  $ab$ -plane, and being isotropic, respectively. A single point calculation has been performed on the obtained slab models, and their density of states is plotted for the various slab layers; see Figure 3.

The DOS across the slab layers obtained from structure 4 is nearly constant along both the [110] and the [001] directions, Figure 3a, with a very small ( $\ll 0.1 \text{ eV}$ ) bending of both the valence and the conduction bands going from the bulk to the outer surface layers. A very different behavior is observed for structures 1 and 3. In the case of structure 1, the DOS along the [110] direction is nearly constant, while along the [001] direction, i.e., the direction with a net alignment of the MA cation, the DOS shows a clear gradient for both the valence and conduction bands, amounting to  $\sim 0.04 \text{ eV}/\text{\AA}$ . The band gap along the [001] direction is nearly constant in all the layers. Finally, the DOS of structure 3, that has a global alignment of the molecules both parallel to the  $ab$ -plane and along the  $c$ -axis, shows a gradient of  $\sim 0.04 \text{ eV}/\text{\AA}$  of the valence and conduction bands along both the [110] and [001] directions. The results clearly point out that, in correspondence of a net alignment of

the MA molecules, the valence and conduction band of the  $\text{MAPbI}_3$  perovskite show a consistent bending, which is reasonably associated with an easier separation of the photogenerated species during the solar cell operational process.<sup>59</sup> This phenomenon, named “*ferroelectric highways*” by Frost et al.,<sup>40</sup> has to deal however with the many structures with different orientations of the MA cations lying within an energy comparable to  $kT$ . It is however interesting to notice the potential of being able to synthesize or grow specifically epitaxially oriented perovskite films as a means to possibly obtain even higher photovoltaic efficiencies. In this regard, McLeod et al. has recently demonstrated that, in the  $\text{MAPbI}_3$  perovskite obtained by the one-step synthesis protocol, the MA cations show a preferential orientation, which is lost in the two-step synthesis.<sup>60</sup>

**3.3. Conversion among Different Structures.** We showed above that many stable structures for tetragonal  $\text{MAPbI}_3$  can exist, lying within an energy range accessible at room temperature, that mainly differ in the orientation of the molecules and/or in the direction of the octahedral tilting (along the [110] rather than the [001] direction). Now, two important questions arise about the actual structure of the  $\text{MAPbI}_3$  crystal: (i) *Is there a single crystal of  $\text{MAPbI}_3$  constituted by just one type of structure, or can two or more structures coexist?* (ii) *How do two differently tilted structures possibly interconvert into each other?*

Dealing with the possible coexistence of more than one local crystal structure, we recall the results of the variable cell optimization of Table 2. We observed that structures 1–7 were predicted with the  $a$  and  $b$  cell parameters shorter than the experiment and the  $c$  parameter longer than the experiment, providing a  $c/a$  ratio of  $\sim 1.46$  against the  $\sim 1.43$  experimental ratio. Structures 8 and 9 instead show the opposite trend, with the  $a$  and  $b$  parameters shorter and the  $c$  parameter longer than the experiment and with a  $c/a$  ratio of  $\sim 1.41$ . Notably, the two different tilting directions are found within less than 0.1 eV per unit cell. Considering the small energetic difference and the fact

that the average cell parameters of structures **1–7** and **8–9** deliver essentially the experimental  $c/a$  ratio, we wonder whether the two types of structure can coexist in a macroscopic sample of  $\text{MAPbI}_3$ . To clarify this point, we simulated the X-ray diffraction pattern of structures **1** and **8**, the former having the octahedral tilting along the [001] direction and the latter along the [110] direction, and we compare them with the experimental data by Stoumpos et al.<sup>29</sup> in Figure 4. Both

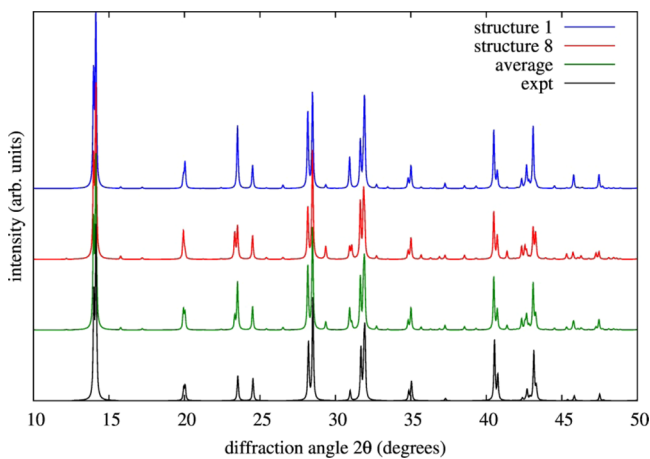


**Figure 4.** Comparison of the experimental X-ray diffraction pattern with the theoretical ones calculated on structures **1** (tilting of the octahedra along the [001] direction) and **8** (tilting of the octahedra along the [110] direction) and their average.

structure **1** and **8** reproduce reasonably well the global experimental pattern, although with some differences. In particular, the X-ray diffraction pattern of structure **1** shows the peaks  $23^\circ$  and  $43^\circ$  with exceedingly high intensity, while structure **8** shows some doublets at  $\sim 23.5^\circ$ ,  $31^\circ$ , and  $42.5^\circ$  that are not found in the experiment.

We have then calculated the average of the X-ray diffraction of structures **1** and **8**, representing the diffraction pattern of a system where domains representative of both structures coexist. This averaged X-ray diffraction pattern seems to match the experimental data to a better extent than those of the individual structures **1** and **8**. The shape of the peak at  $20^\circ$  is predicted in better agreement with the experiment, as well as the relative intensity of the doublet at  $23\text{--}24^\circ$  and the complex signal at  $43^\circ$ . Thus, the possibility to have different crystalline domains, with octahedral tilting along different directions, sufficiently large to provide a well-defined X-ray diffraction signal, seems consistent with the experimental X-ray diffraction pattern.

To further investigate on the coexistence of various different structures, we constructed an ad hoc model constituted by two crystalline cells, based on the optimized structures **1** and **8**, stacked along the [001] direction (see Figure 5). We have optimized this mixed structure both with the fixed, experimental cell parameters and the variable ones, using a consistent  $4 \times 4 \times 2$  k-point mesh. Notably, the mixed structure retained the original structure with two different tiltings in the different cells. Employing the experimental cell parameters, the band gap of this system (1.54 and 0.42 eV by SR- and SOC-DFT, respectively) is slightly smaller than those of the parent structures **1** (1.57/0.53 eV) and **8** (1.60/0.46 eV). Considering relaxation of atomic and cell parameters, the band gap of the mixed system (1.49 eV) is close to the band gap of structure **1** (1.47 eV). Notably, the calculated cell parameters

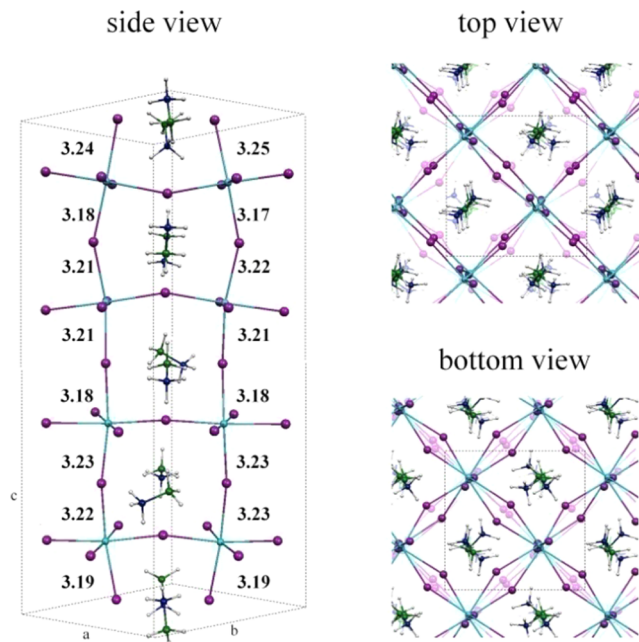


**Figure 5.** Optimized structure of the mixed structure obtained by combining structures **1** and **8**.

are now in better agreement with the experimental data, with a  $c/a$  ratio of  $\sim 1.43$  ( $a = 8.81 \text{ \AA}$ ,  $b = 8.80 \text{ \AA}$ ,  $c = 12.64 \text{ \AA}$ ), as experimentally found. The present system is calculated to be 0.16 eV less stable than the structure **1** (doubled along the  $c$  axis and reoptimized with a  $k = 4 \times 4 \times 2$  point mesh) at the experimental cell parameters (0.22 eV with the optimized parameters). Considering the small energetic difference and the fact that the average cell parameters of structures **1–7** and **8–9** deliver essentially the experimental  $c/a$  ratio, we propose that the  $\text{MAPbI}_3$  material may possibly be constituted by domains of alternating tilting directions which may further dynamically interconvert into each other at room temperature. The picture extracted from our calculations is likely to be consistent with the measurements by Choi et al.,<sup>61</sup> who found small crystalline domains composed by roughly one  $\text{MAPbI}_3$  unit cell.

We now wish to deal with the mechanism driving the transition among the different investigated structures. Experimental investigations have previously demonstrated that the orientational dynamics of the MA cations takes place in the picosecond time scale.<sup>7,36</sup> On the other hand, we found many possible structures in an energy range of a few kT, that are therefore accessible to portions of the  $\text{MAPbI}_3$  at room temperature. The point is thus how a random rotational motion of the MA cations, in the picosecond time scale, can be related to the presence of the stable structures we calculate and how the transition among these structures can possibly take place.

To clarify these points, we have considered various interconversion pathways between two different structures. In this case, we have considered the conversion between structures **1** and **9**, being representative of polar/apolar structures with the octahedral tilting along the [001] and the [110] directions, respectively. Here, we have considered the following transitions: (a) the inorganic atoms follow a synchronous linear path, connecting the starting and the final structure, with the MA cations free to relax at each optimization step; (b) same as (a) but with the MA cations substituted by  $\text{Cs}^+$  ions; and (c) a stepwise pathway in which one MA molecule at the time of

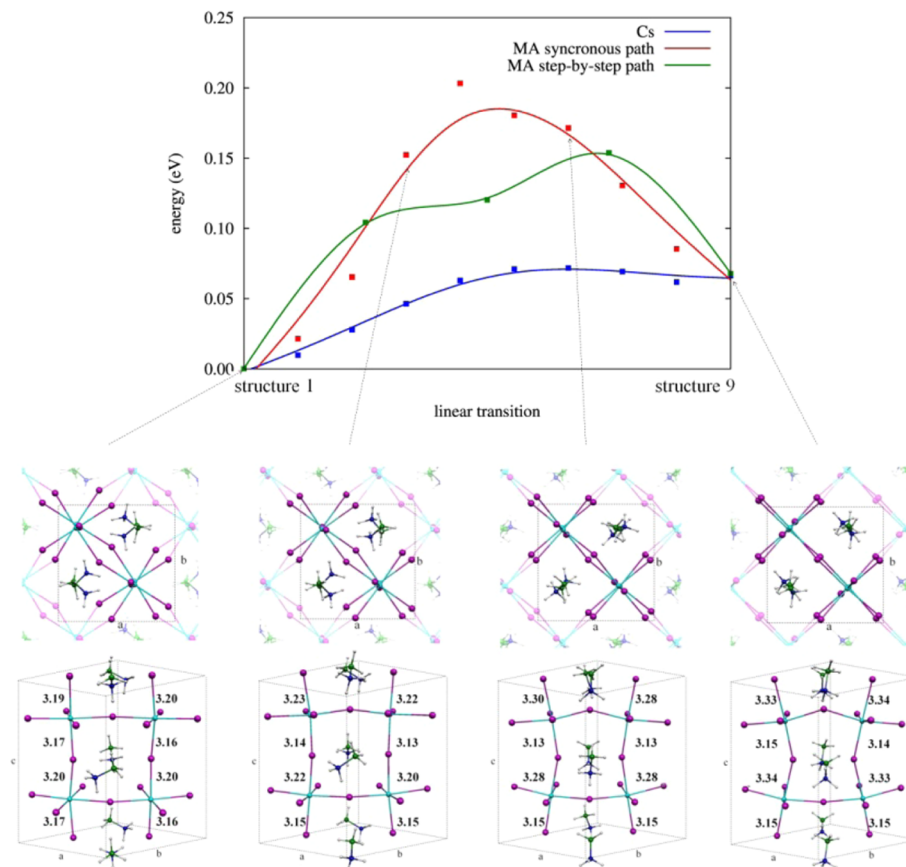


**Figure 6.** Possible mechanisms for the conversion from structure 1 (tilting along the [001] direction) to structure 9 (tilting along the [110] direction). Synchronous transition with Cs cations in place of the MA cations (blue line); synchronous transition with the MA cation (red line); MA stepwise transition (green line).

the starting structure is rotated in the corresponding orientation of the final orientation and all the other atoms are allowed to relax. These calculations, whose results are reported in Figure 6, are carried out with cell parameters fixed to the experimental values. In the cases (a) and (c), i.e., when the MA cations are considered to rotate in a synchronous or stepwise pathway, we calculate energy barriers of 0.22 and 0.15 eV, respectively. In the (b) case, i.e., when MA is replaced by Cs+, the process is essentially barrierless. It is thus clear that the presence of an energetic barrier is due to the specific interaction between the MA cations and the inorganic framework. In particular, during the transition among the two considered structures in the presence of the MA cations, the system passes through some configurations with an unfavorable hydrogen bond pattern, which are less stable than the starting and final structures. It is worth mentioning that in the case (c), where the stepwise pattern was followed, the orientation of each molecule was preserved during the optimization.

In light of the calculated lower barrier, a conversion driven by a stepwise succession of rotations of the MA cations seems the most likely process in the case of a thermally driven transition. It is worth noting, however, that this conversion mechanism is dictated by a more or less random rotation of the MA cations and thus it is reasonably a slow process, with respect to the MA rotation time-scale ( $\sim$ few ps).<sup>7,36</sup> At the opposite, the synchronous rearrangement of the atoms from one structure to the other is more likely when an external electric field is imposed to the material, which decreases the transition barrier and makes the potential felt by the MA cations anisotropic, thus

leading to a synchronous rearrangement of the material. Nevertheless, in light of the large barriers to the transition, a slower transition mechanism (with respect to the MA rotation time-scale) is expected. This is consistent with the results from Snaith et al., who observed a hysteresis in the current–potential curve of the  $\text{MAPbI}_3$  which became more marked at slow potential scanning rate ( $\sim$ 0.001 V/s).<sup>62</sup> Within this time scale, in fact, enough time is probably given to the material to rearrange to the new external potential.

It is also worth comparing our results with recent data by Savenije et al.,<sup>63</sup> who showed a thermally activated process to charge recombination in tetragonal  $\text{MAPbI}_3$ , with a characteristic barrier of 0.075 eV, which the authors partly attributed to the rotational barrier of the MA cations. The measured barrier, determined under light irradiation, is definitely consistent with our estimate calculated for the ground state, also considering the anticipated enhanced MA rotational freedom in the excited state.<sup>64</sup>

**3.4. Dynamics in Polar and Apolar Structures.** All the previous results and considerations were based on the results of static DFT calculations, which showed rotational barriers of the order of  $\sim$ 0.2 eV. Nevertheless, such energy is accessible to a (reasonably) small part of the system also at room temperature. Thus, to investigate the actual dynamics of the system, in particular of the MA cations, in conditions closer to the operative ones, we have carried out Car–Parrinello molecular dynamics simulations. Such simulations are expected to unveil the rotational dynamics of the MA cations and its possible role in the transition among the possible stable structures of the

$\text{MAPbI}_3$ . Here, we have considered a  $2 \times 2 \times 2$  supercell of structures **1** and **4**, being respectively representative of the ferroelectric-like and of the antiferroelectric-like structures, to investigate on the possible differences.

In Figure 7, we compare the radial distribution function (RDF) for the inorganic component obtained from the CPMD

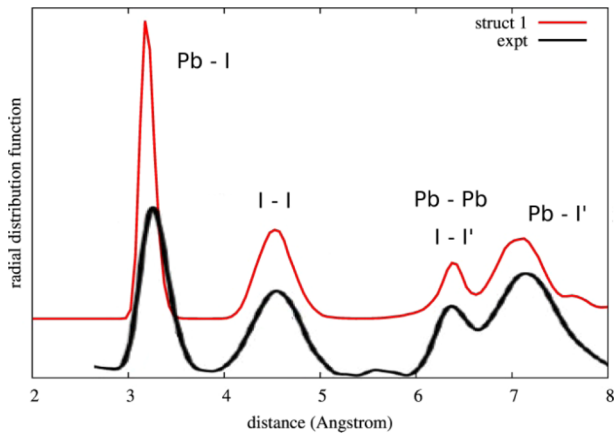


**Figure 7.** Radial distribution function (RDF) calculated from the CPMD simulation of structure **1** compared with the experimental data from ref 61. The height of the experimental RDF has been rescaled to fit the theoretical peak at  $\sim 4.4$  Å.

simulation on the structure **1**, with the experimental data.<sup>61</sup> The theoretical RDF parallels very well the experiment, both in peak positions and broadening, demonstrating the reliability of our simulations in relation to both the average structure and on the atomic dynamical displacement. The CPMD satisfactorily reproduces the first two peaks at  $\sim 3.2$  Å and  $\sim 4.4$  Å, even if our theoretical simulation predicts a narrower peak associated with the Pb–I bond with respect to the experiment. The RDF reproduces satisfactorily also the peaks at 6.4 and 7.1 Å.

In Figure 8 we report the distribution of the  $\phi$  and  $\theta$  angles during the CPMD dynamics for the investigated structures **1** and **4**. In both cases, the  $\phi$  and  $\theta$  angles have maxima in correspondence of the orientation of the optimized structures (see Table 1); thus, under the dynamics conditions and time

scale, the MA cations tend to preserve the favored orientations depicted in Scheme 1. However, significant differences are observed in the width of the distributions and in correspondence of the minima of the angles distributions. A tail in the distribution of  $\phi$  is observed for the case of structure **4**, while this is completely absent in the case of structure **1**. Similarly, in structure **4** the molecules explore configurations in the middle, the most probable orientations within the *ab*-plane (see Scheme 1), i.e.,  $\theta = 0, 180, 270, 360^\circ$ , while this does not happen in the case of structure **1**.

We now focus more in detail on the evolution of the orientation of the MA cations in the two investigated structures, following the evolution of the  $\theta$  and  $\phi$  angles during the dynamics for each of the 32 MA molecules. In the case of structure **1**, the molecules do not reorient during the 12 ps dynamics, keeping the original orientation, consistently with the absence of orientations at  $\theta = 0^\circ, 90^\circ, 180^\circ$ , and  $270^\circ$  in Figure 8. The ferroelectric-like structure **1** is thus a stable structure that does not show any structural evolution within the considered time-scale. It is also possible that finite size effects, due to the employed  $2 \times 2 \times 2$  replicated cell, may contribute to “lock” structure **1** in its starting configuration.<sup>65</sup>

In the case of structure **4** instead, four molecules rotate from their original orientation during the 12 ps dynamics. In Figure 9, we report the evolution of  $\phi$  and  $\theta$  for one rotating molecule, which rotates from the  $-B$  to the  $+A$  configuration (see Scheme 1). During the rotation, this molecule changes both its orientation within the *ab*-plane (i.e.,  $\theta$ ) and tilting (i.e.,  $\phi$ ) in a concerted fashion. The same behavior has been found for all four reorienting molecules we observed during structure **4** dynamics. Thus, *rotation of the MA cations requires a coupled reorientation within the ab-plane and the concerted modification of the tilting with respect to it*. It seems reasonable to associate this fact to the peculiar shape of the  $a^0a^0c^-$  tilted inorganic framework, which is nearly invariant for an  $S_4$  improper rotation axis. It is also worth noting that the measured time-scale of the molecular rotation in the  $\text{MAPbI}_3$  is of the order of a few picoseconds, in good keeping with the experimental data available in the literature. On average, we observe that the values of the  $\phi$  and  $\theta$  averaged over all the 32 molecules of the model do not deviate significantly from the starting values ( $0^\circ$

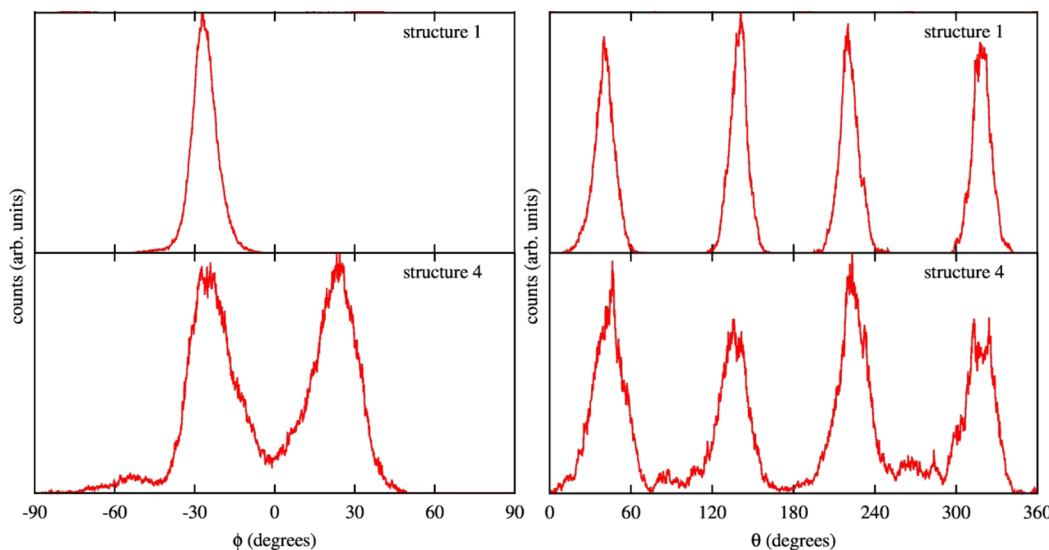


**Figure 8.** Distribution of the  $\phi$  (left) and  $\theta$  (right) angles, as defined in Scheme 1, during the CPMD simulation for structures **1** and **4**.

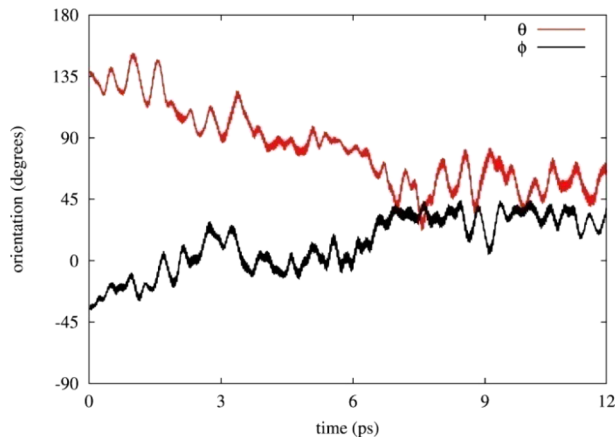


**Figure 9.** Evolution of the  $\theta$  and  $\phi$  angles for a selected rotating MA molecule from the CPMD simulation of structure 4.

and  $180^\circ$ ); thus, in spite of the greater mobility of the molecules in the present system, we do not observe a transition toward the more stable structure 1 within the investigated time scale. Nevertheless, it is meaningful to observe that the present system is far more flexible than the ferroelectric-like structure 1. The mean molecular orientation in structure 4, averaged over all the 32 cations of the model, shows that after 3 ps the molecules tilt with respect to the *ab*-plane (see Supporting Information Figure SI2).

As a final check of the impact of the atoms dynamic on the electronic structure of the tetragonal  $\text{MAPbI}_3$  perovskite, we report in Figure 10 the time evolution of the highest occupied

seen in Figure 10. This is likely to be related to the larger cuboctahedral cavities typical of the cubic compared to the tetragonal phase, leaving more space for cation rotation.

#### 4. CONCLUDING REMARKS

We have reported the results of ab initio electronic structure and Car–Parrinello molecular dynamics simulations on several structural models of the prototype  $\text{MAPbI}_3$  perovskite for solar cell applications. We considered both configurations having a preferred orientation of the MA cations, giving rise to a net dipole alignment, and configurations with an isotropic distribution of the MA cations, the former and latter likely being representative of polar (ferroelectric) and apolar (antiferroelectric) structures. Our calculations demonstrate the preferred stability of a set of polar structures over apolar ones, with an energy difference within 0.1 eV and a conversion barrier within 0.2 eV per unit cell (four  $\text{MAPbI}_3$  units), thus possibly accessible at room temperature. Notably, within the same energy range, we calculate structures having the typical octahedra tilting around the [001] direction, of  $a^0a^0c^-$  type according to the Glazer notation, and with tilting along the [110] direction. The two types of octahedra tilting give rise to different calculated  $c/a$  ratios, with a mixed structure having tilting along both directions providing an improved agreement with simulated X-ray diffraction patterns.

The most stable structures show an ordered angle (of  $\sim 30^\circ$ ) of the MA cations with respect to the *ab*-plane, thus exhibiting a net dipole along the [001] direction. No preferential orientations with respect to the four possible orientations in the *ab*-plane were instead found, consistently with the observed tetragonal unit cell. It is worth noting that, as a consequence of the ferroelectric-like or antiferroelectric-like orientation of the MA cations, the inorganic framework shows a different pattern of bond length alternation along the *c*-axis. Ferroelectric-like orientations impose a quasi  $I4cm$  structure for the inorganic component, characterized by lack of inversion symmetry, while the antiferroelectric-like orientations impose a quasi  $I4/mcm$  structure.

Ab initio molecular dynamics simulations demonstrate that the stability of the ferroelectric-like structures is not affected by thermal effects. From 12 ps CPMD simulations carried out at  $\sim 320$  K, we observe that the considered ferroelectric-like structure is quite rigid, showing no molecular rotations in the investigated time scale. At the opposite, the considered antiferroelectric-like structure is more flexible, with several rotating molecules in the investigated time scale, reflecting its slightly higher energy.

The two  $I4cm$  and  $I4/mcm$  types of structure have markedly different electronic properties, despite showing a relatively small band gap variation. In particular, the  $I4cm$ -like structures exhibit a notable Rashba/Dresselhaus effect, which is forbidden by selection rules in the  $I4/mcm$ -like structures characterized by inversion symmetry. The entity and direction of this effect is modulated by the orientation of the MA cations, suggesting a strong interplay of orientational order and electronic structure in organohalide perovskites. The possible role of a Rashba/Dresselhaus effect on the photovoltaic operation is still to be understood in detail, although it is likely this might slow down recombination of charge carriers. Simulations carried out on finite surface slabs demonstrate that a net orientation of the MA cations gives rise to a strong bending in the valence and conduction bands, which could definitely assist charge separation and reduce carrier recombination.

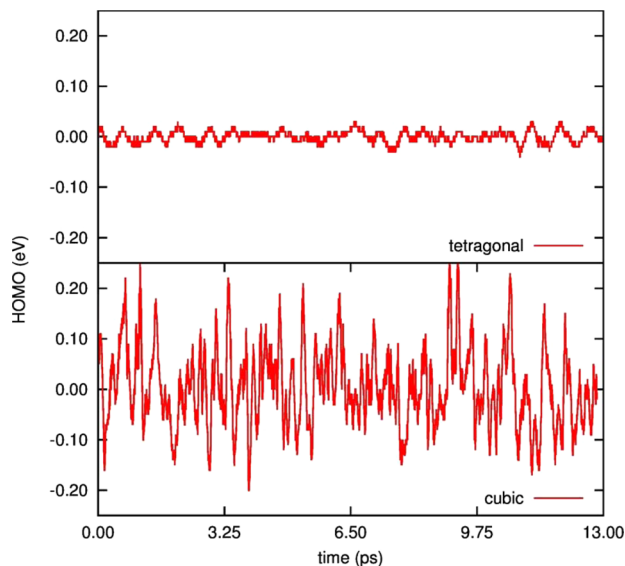


**Figure 10.** Time evolution of the HOMO for the tetragonal (upper panel) and cubic (lower panel)  $\text{MAPbI}_3$  perovskite.

molecular orbital (HOMO) obtained from CPMD calculations as a function of the simulation time comparing it with the previously reported data for the cubic structure.<sup>21</sup>

As it can be noticed from Figure 10, the cubic phase exhibits much wider oscillations in the energy levels than the oriented tetragonal structure 1, reflecting the narrower distribution of MA cation orientations found in the latter. In particular, while for the cubic structure we found a HOMO standard deviation of 0.08 eV, in structure 1 this amounts to 0.01 eV, as clearly

In summary, we have demonstrated that the most stable structure of the  $\text{MAPbI}_3$  perovskite shows a preferential orientation of the MA cations along the [001] direction. We have also demonstrated, however, that within 0.1 eV the system can access both apolar structures, with no net MA dipole resultant, and structures characterized by tilting of the  $\text{PbI}_6$  octahedra along both the [001] and [110] directions. Our results are fully consistent with the degree of medium range disorder exhibited by  $\text{MAPbI}_3$  in its tetragonal phase and provide an energetic figure for the possible effects of preferential cation orientation in this material. On the basis of the calculated structural variability, conversion barrier among different structures, and structural energetics, it is likely that the material will not exhibit a unique structural type but rather will be constituted by domains which may further dynamically interconvert into each other at room temperature, giving rise to the observed average materials properties. We believe the present results could contribute an important step toward an in-depth comprehension of the basic properties of organohalide perovskites, assisting a further optimization of their photovoltaic response.

## ■ ASSOCIATED CONTENT

### S Supporting Information

Additional data and tables. This material is available free of charge via the Internet at <http://pubs.acs.org>.

## ■ AUTHOR INFORMATION

### Corresponding Author

\*(F.D.A.) E-mail: filippo@thch.unipg.it.

### Author Contributions

<sup>§</sup>C.Q. and E.M. contributed equally to this work.

### Notes

The authors declare no competing financial interest.

## ■ ACKNOWLEDGMENTS

The research leading to these results has received funding from the European Union Seventh Framework Programme [FP7/2007%2013] under Grant Agreement No. 604032 of the MESO project.

## ■ REFERENCES

- (1) Tanaka, K.; Takahashi, T.; Ban, T.; Kondo, T.; Uchida, K.; Miura, N. *Solid State Commun.* **2003**, *127*, 619–623.
- (2) Stranks, S. D.; Eperon, G. E.; Grancini, G.; Menelaou, C.; Alcocer, M. J. P.; Leijtens, T.; Herz, L. M.; Petrozza, A.; Snaith, H. J. *Science* **2013**, *334*, 341–344.
- (3) Xing, G.; Mathews, N.; Sun, S.; Lim, S. S.; Lam, Y. M.; Graetzel, M.; Mhaisalkar, S.; Sum, T. C. *Science* **2013**, *342*, 344–347.
- (4) Wehrenfennig, C.; Eperon, G. E.; Johnston, M. B.; Snaith, H. J.; Herz, L. M. *Adv. Mater.* **2014**, *26*, 1584–1589.
- (5) Ponseca, C. S.; Savenije, T. J.; Abdellah, M.; Zheng, K.; Yartsev, A.; Pascher, T.; Harlang, T.; Chabera, P.; Pullerits, T.; Stepanov, A.; et al. *J. Am. Chem. Soc.* **2014**, *136*, 5189–5192.
- (6) Wehrenfennig, C.; Liu, M.; Snaith, H. J.; Johnston, M. B.; Herz, L. M. *Energy Environ. Sci.* **2014**, *7*, 2269–2275.
- (7) Poglitsch, A.; Weber, D. *J. Chem. Phys.* **1987**, *87*, 6373–6378.
- (8) Kojima, A.; Teshima, K.; Shirai, Y.; Miyasaka, T. *J. Am. Chem. Soc.* **2009**, *131*, 6050–6051.
- (9) Im, J.-H.; Lee, C.-R.; Lee, J.-W.; Park, S.-W.; Park, N.-G. *Nanoscale* **2011**, *3*, 4088–4093.
- (10) Etgar, L.; Gao, P.; Xue, Z.; Peng, Q.; Chandiran, A. K.; Liu, B.; Nazeeruddin, M. K.; Grätzel, M. *J. Am. Chem. Soc.* **2012**, *134*, 17396–17399.
- (11) Lee, M. M.; Teuscher, J.; Miyasaka, T.; Murakami, T. N.; Snaith, H. J. *Science* **2012**, *338*, 463–467.
- (12) Abrusci, A.; Stranks, S. D.; Docampo, P.; Yip, H.-L.; Jen, A. K.-Y.; Snaith, H. J. *Nano Lett.* **2013**, *13*, 3124–3128.
- (13) Burschka, J.; Pellet, N.; Moon, S. J.; Humphry-Baker, R.; Gao, P.; Nazeeruddin, M. K.; Graetzel, M. *Nature* **2013**, *499*, 316–319.
- (14) Crossland, E. J. W.; Noel, N.; Sivaram, V.; Leijtens, T.; Alexander-Webber, J. A.; Snaith, H. J. *Nature* **2013**, *495*, 215–219.
- (15) Edri, E.; Kirmayer, S.; Cahen, D.; Hodes, G. *J. Phys. Chem. Lett.* **2013**, *4*, 897–902.
- (16) Heo, J. H.; Im, S. H.; Noh, J. H.; Mandal, T. N.; Lim, C.-S.; Chang, J. A.; Lee, Y. H.; Kim, H.-j.; Sarkar, A.; Nazeeruddin, M. K.; et al. *Nat. Photonics* **2013**, *7*, 486–491.
- (17) Liu, M.; Johnston, M. B.; Snaith, H. J. *Nature* **2013**, *501*, 395–398.
- (18) Lv, S.; Pang, S.; Zhou, Y.; Padture, N. P.; Hu, H.; Wang, L.; Zhou, X.; Huimin, Z.; Zhang, L.; Huang, C.; et al. *Phys. Chem. Chem. Phys.* **2014**, *16*, 19206–19211.
- (19) Hanusch, F. C.; Wiesenmayer, E.; Mankel, E.; Binek, A.; Angloher, P.; Fraunhofer, C.; Giesbrecht, N.; Feckl, J. M.; Jaegermann, W.; Johrendt, D.; et al. *J. Phys. Chem. Lett.* **2014**, *5*, 2791–2795.
- (20) Quarti, C.; Grancini, G.; Mosconi, E.; Bruno, P.; Ball, J. M.; Lee, M. M.; Snaith, H. J.; Petrozza, A.; Angelis, F. D. *J. Phys. Chem. Lett.* **2014**, *5*, 279–284.
- (21) Mosconi, E.; Quarti, C.; Ivanovska, T.; Ruani, G.; De Angelis, F. *Phys. Chem. Chem. Phys.* **2014**, *16*, 16137–16144.
- (22) D’Innocenzo, V.; Grancini, G.; Alcocer, M. J. P.; Kandada, A. R. S.; Stranks, S. D.; Lee, M. M.; Lanzani, G.; Snaith, H. J.; Petrozza, A. *Nat. Commun.* **2014**, *5*, 3586.
- (23) Umebayashi, T.; Asai, K.; Kondo, T.; Nakao, A. *Phys. Rev. B* **2003**, *67*, 155405.
- (24) Chang, Y. H.; Park, C. H. *J. Korean Phys. Soc.* **2004**, *44*, 16137–16144.
- (25) Mosconi, E.; Amat, A.; Nazeeruddin, M. K.; Graetzel, M.; De Angelis, F. *J. Phys. Chem. C* **2013**, *117*, 13902–13913.
- (26) Onoda-Yamamoto, N.; Matsuo, T.; Suga, H. *J. Phys. Chem. Solids* **1992**, *53*, 935–939.
- (27) Brivio, F.; Walker, A. B.; Walsh, A. *Appl. Phys. Lett.* **2013**, *102*, 042111/1–042111/5.
- (28) Amat, A.; Mosconi, E.; Ronca, E.; Quarti, C.; Umari, P.; Nazeeruddin, M. K.; Grätzel, M.; Angelis, F. D. *Nano Lett.* **2014**, *14*, 3608–3616.
- (29) Stoumpos, C. C.; Malliakas, C. D.; Kanatzidis, M. G. *Inorg. Chem.* **2013**, *52*, 9019–9038.
- (30) Kutes, Y.; Ye, L.; Zhou, Y.; Pang, S.; Huey, B. D.; Padture, N. P. *J. Phys. Chem. Lett.* **2014**, *5*, 3335–3339.
- (31) Grinberg, I.; West, D. V.; Torres, M.; Gou, G.; Stein, D. M.; Wu, L.; Chen, G.; Gallo, E. M.; Akbashev, A. R.; Davies, P. K.; et al. *Nature* **2013**, *503*, 509–512.
- (32) Wang, F.; Grinberg, I.; Rappe, A. M. *Appl. Phys. Lett.* **2014**, *104*, 152903.
- (33) Swainson, I. P.; Hammond, R. P.; Soulliére, C.; Knop, O.; Massa, W. *J. Solid State Chem.* **2003**, *176*, 97–104.
- (34) Chi, L.; Swainson, I.; Cranswick, L.; Her, J.-H.; Stephens, P.; Knop, O. *J. Solid State Chem.* **2005**, *178*, 1376–1385.
- (35) Baikie, T.; Fang, Y.; Kadro, J. M.; Schreyer, M.; Wei, F.; Mhaisalkar, S. G.; Graetzel, M.; White, T. J. *J. Mater. Chem. A* **2013**, *1*, 5628–5641.
- (36) Wasylshen, R. E.; Knop, O.; MacDonald, J. B. *Solid State Commun.* **1985**, *56*, 581–582.
- (37) Yukihiro, K.; Hiroyuki, M.; Hasebe, K. *J. Phys. Soc. Jpn.* **2002**, *71*, 1694–1697.
- (38) Glazer, A. M. *Acta Crystallogr.* **1972**, *B28*, 3384–3391.
- (39) Brivio, F.; Butler, K. T.; Walsh, A.; van Schilfgaarde, M. *Phys. Rev. B* **2014**, *89*, 155204/1–155204/6.
- (40) Frost, J. M.; Butler, K. T.; Brivio, F.; Hendon, C. H.; van Schilfgaarde, M.; Walsh, A. *Nano Lett.* **2014**, *14*, 2584–2590.
- (41) Giorgi, G.; Fujisawa, J.-I.; Segawa, H.; Yamashita, K. *J. Phys. Chem. Lett.* **2013**, *4*, 4213–4216.

- (42) Giorgi, G.; Fujisawa, J.-I.; Segawa, H.; Yamashita, K. *J. Phys. Chem. C* **2014**, *118*, 12176–12186.
- (43) Even, J.; Pedesseau, L.; Jancu, J.-M.; Katan, C. *J. Phys. Chem. Lett.* **2013**, *4*, 2999–3005.
- (44) Kim, M.; Im, J.; Freeman, A. J.; Ihm, J.; Jin, H. *Proc. Natl. Acad. Sci. U.S.A.* **2014**, *111*, 6900–6904.
- (45) Worhatch, R. J.; Kim, H.; Swainson, I. P.; Yonkeu, A. L.; Billinge, S. J. L. *Chem. Mater.* **2008**, *20*, 1272–1277.
- (46) Colella, S.; Mosconi, E.; Fedeli, P.; Listorti, A.; Gazza, F.; Orlandi, F.; Ferro, P.; Besagni, T.; Rizzo, A.; Calestani, G.; et al. *Chem. Mater.* **2013**, *25*, 4613–4618.
- (47) Filippetti, A.; Mattoni, A. *Phys. Rev. B* **2014**, *89*, 125203/1–8.
- (48) Giannozzi, P.; Baroni, S.; Bonini, N.; Calandra, M.; Car, R.; Cavazzoni, C.; Ceresoli, D.; Chiarotti, G. L.; Cococcioni, M.; Dabo, I.; et al. *J. Phys.: Condens. Matter* **2009**, *21*, 395502.
- (49) Perdew, J. P.; Burke, K.; Ernzerhof, M. *Phys. Rev. B* **1996**, *77*, 3865–3868.
- (50) Vanderbilt, D. *Phys. Rev. B* **1990**, *41*, 7892–7895.
- (51) Pasquarello, A.; Laasonen, K.; Car, R.; Lee, C.; Vanderbilt, D. *Phys. Rev. Lett.* **1992**, *69*, 1982–1985.
- (52) Giannozzi, P.; De Angelis, F.; Car, R. *J. Chem. Phys.* **2004**, *120*, 5903–5915.
- (53) Umari, P.; Mosconi, E.; De Angelis, F. *Sci. Rep.* **2014**, *4*, 4467/1–4467/4.
- (54) Geng, W.; Zhang, L.; Zhang, Y.-N.; Lau, W.-M.; Liu, L.-M. *J. Phys. Chem. C* **2014**, *118*, 19565–19571.
- (55) Egger, D. A.; Kronik, L. *J. Phys. Chem. Lett.* **2014**, *5*, 2728–2733.
- (56) Wang, Y.; Gould, T.; Dobson, J. F.; Zhang, H.; Yang, H.; Yao, X.; Zhao, H. *Phys. Chem. Chem. Phys.* **2014**, *16*, 1424–1429.
- (57) Menéndez-Proupin, E.; Palacios, P.; Wahnón, P.; Conesa, J. C. *Phys. Rev. B* **2014**, *90*, 045207.
- (58) Szczęśniak, M. M.; Bernstein, R. J.; Cybulski, S. M.; Scheiner, S. *J. Phys. Chem.* **1990**, *94*, 1781–1788.
- (59) Laban, W. A.; Etgar, L. *Energy Environ. Sci.* **2013**, *6*, 3249–3253.
- (60) McLeod, J. A.; Wu, Z.; Shen, P.; Sun, B.; Liu, L. *J. Phys. Chem. Lett.* **2014**, *5*, 2863–2867.
- (61) Choi, J. J.; Yang, X.; Norman, Z. M.; Billinge, S. J. L.; Owen, J. S. *Nano Lett.* **2013**, *14*, 127–133.
- (62) Snaith, H. J.; Abate, A.; Ball, J. M.; Eperon, G. E.; Leijtens, T.; Noel, N. K.; Stranks, S. D.; Wang, J. T.-S.; Wojciechowski, K.; Zhang, W. *J. Phys. Chem. Lett.* **2014**, *5*, 1511–1515.
- (63) Savenije, T. J.; Ponseca, C. S.; Kunnenman, L.; Abdellah, M.; Zheng, K.; Tian, Y.; Zhu, Q.; Canton, S. E.; Scheblykin, I. G.; Pullerits, T.; et al. *J. Phys. Chem. Lett.* **2014**, *5*, 2189–2194.
- (64) Gottesman, R.; Haltzi, E.; Gouda, L.; Tirosh, S.; Bouhadana, Y.; Zaban, A.; Mosconi, E.; De Angelis, F. *J. Phys. Chem. Lett.* **2014**, *5*, 2662–2669.
- (65) Carignano, M. A.; Kachmar, A.; Hutter, J. Thermal Effects on  $\text{CH}_3\text{NH}_3\text{PbI}_3$  Perovskite from *Ab-initio* Molecular Dynamics Simulations. *arXiv:1409.6842*, **2014**.